

Research Article

Dynamic Mechanical Response, Cracking Behavior, and Stress Intensity Factors of Cement Mortar Specimens with Open and Closed Flaws

Qizhi Wang,¹ Fangshi Shi,¹ Xiao Wang,¹ Qingling Meng ,² Xing Li ,³ Jinbo Song,⁴ and Chang-yi Yu⁵

¹School of Civil Engineering, Hebei University of Science and Technology, Shijiazhuang 050018, China

²School of Civil Engineering, Tianjin Chengjian University, Tianjin 300384, China

³Department of Civil & Mineral Engineering, University of Toronto, Toronto, ON M5S 1A4, Canada

⁴School of Civil Engineering, Jiangxi Communications Vocational and Technical College, Nanchang 330013, China

⁵CCCC First Harbor Engineering Company, Co. Ltd., Tianjin 300461, China

Correspondence should be addressed to Qingling Meng; mql-d163@163.com and Xing Li; xingmail.li@utoronto.ca

Received 6 September 2021; Revised 29 October 2021; Accepted 19 November 2021; Published 27 February 2022

Academic Editor: Bangbiao Wu

Copyright © 2022 Qizhi Wang et al. This is an open access article distributed under the Creative Commons Attribution License, which permits unrestricted use, distribution, and reproduction in any medium, provided the original work is properly cited.

Major civil and military infrastructures are usually located in mountainous areas with complex geological structures. When subjected to impact loads caused by operational blasting or seismic activities, the inherent flaws or joints in the hosting rock mass may grow irreversibly and eventually cause the entire structure to collapse. It is, therefore, desirable to understand the mechanical and cracking behaviors of flawed rock structures under dynamic loads. In this work, the cement mortar is used to make the plate specimens, and two different types of flaws, i.e., the open and the closed (resin-filled) flaws, with different inclination angles from 0° to 90° with respect to the loading direction are prefabricated. The nominal strength, crack initiation, and failure characteristics of the specimens under different loading rates are investigated using the split Hopkinson bar (SHPB) system in conjunction with the digital image correlation (DIC) technique. The results indicate that the dynamic nominal strength of both two types of specimens shows similar loading rate and flaw angle dependency, specifically, monotonically increasing with the increase of the loading rate while increasing first and then decreasing with increasing the flaw inclination angle. The strength of specimens with an open flaw is obviously lower than that of the specimens with a closed flaw at a similar loading rate. Besides, the failure mode of specimens with an open flaw is mainly an X-shaped tensile or tensile-shear mixed form regardless of the flaw inclination, whereas the resin-filled flawed specimens always fail in the form of an atypical X-shaped shear pattern with obvious randomness. Moreover, the stress field around the crack tip is carefully extracted based on the obtained displacement field from DIC analysis; the stress intensity factors at crack initiation onset also show flaw inclination- and loading rate-dependent behavior. The strength, cracking behavior, and stress field around the tip during the dynamic loading are closely related to the friction effect between the flaw surfaces. The findings in this work provide some basic insights into the cracking mechanism of rock with open and closed flaws under dynamic loading conditions.

1. Introduction

Rock masses are generally discontinuous at various scales due to the presence of faults, joints, fissures, partings, flaws, and any other inherent defects formed during the diagenesis process and geological-tectonic evolution [1–3]. When

subjected to external loading, these discontinuities may be activated and uncontrollably developed, further leading to the ultimate collapse of the entire rock structure. Hence, the understanding of mechanical responses and fracture mechanisms of rocks with discontinuities is crucial in evaluating the stability of the geostructures. Considering the

difficulties in monitoring in situ stress distribution and detecting the fracture characteristics in field, the flawed raw rock or rock-like materials with prefabricated flaws are commonly adopted as an alternative approach to reproduce the fracture process in laboratory studies [2–14].

To date, the influences of various experimental parameters such as the loading conditions [2–4, 7, 15, 16], rock types [17, 18], and flaw properties (i.e., open and closed flaws, geometries, and quantities) [4, 14, 19–21] on the mechanical and cracking properties of the flawed rock have been extensively investigated using the experimental and numerical methods, and many significant findings have been revealed. Typically, the overall compressive strength of the flawed rock is significantly lower than that of the intact rock at similar loading conditions [5], and the flaw inclination angle can significantly affect the crack initiation position, propagation angles, and even the propagation priority [21]. Besides, the crack coalescence pattern is also affected by the confining pressure. Under high confining pressure conditions, antiwing cracks were often observed, and the confining pressure effect is dominated in determining the failure mode [15, 22]. Moreover, considering the flaw in practical rock engineering is often infilled, some efforts have been devoted to studying the effect of the closed flaws on the fracturing process [9, 19, 23–25]. Their results demonstrate that the cracking behaviors are obviously different between closed and open flaws, and the overall strength, initiation, and coalescence stresses for closed flaws are higher than those of the open flaws due to the friction effect and the stress transmission capacity.

The aforementioned investigations are mainly focused on the mechanical and failure properties of flawed rocks under static stress conditions, whereas in real rock engineering the external loads induced by the operational blasting or seismic activities are fundamentally dynamic. The mechanical responses of the flawed rock and the flaws under dynamic loading are different from those under static or quasistatic stress conditions, and the damage formed in rock at high loading rates can hardly be manifested by reloading at low loading rates [26]. Li and Wong [21] pointed out that the loading rate could affect the crack initiation sequence and the mechanical mechanism based on the stress wave propagation theory was also analyzed. Later, Zhang and Wong [27] investigated the stress variations enclosing the crack tips, stress-strain curves, and the coalescence stress and mode under various loading rates. Generally, both the crack initiation and the peak stresses increased linearly with increasing the loading rate [28], and the cracks' coalescence pattern gradually changed from tensile-segments-dominant to shear-band-dominant as the loading rate increased. Moreover, Li et al. [29] conducted the dynamic compressive test of single and double flawed marble using the split Hopkinson pressure bar (SHPB) system and suggested that an optimized arrangement of the flaws could significantly improve the fragmentation efficiency. However, the existing studies are mostly limited to qualitatively describing the effects of the loading rate on cracking process and nominal mechanical properties of the rock with open flaws, whereas some essential issues such as

the quantitative analysis of the stress field around the crack tip, the cracking mechanism, and even the cracking behavior of the infilled flaws under dynamic loading conditions are rarely involved.

In order to describe the initiation, propagation, and coalescence process of the flaws, various monitoring approaches such as direct photographic snapshot with high-speed cameras [5, 29–31], numerical simulation techniques [17–20, 32–34], microcomputed tomography (micro-CT) scanning [15, 22], acoustic emission (AE) location [35–37], and digital image correlation (DIC) method [32, 38] have been widely adopted. Among them, the DIC method has particular advantages in quantitatively characterizing the full-field displacement and strain fields, based on which more mechanical and fracture parameters can be accurately determined, and thus, more in-depth information with regard to real-time cracking behaviors and cracking mechanisms can be revealed. For example, Gao et al. [39, 40] obtained the fracture propagation parameters such as the location of the crack tip, propagation velocity, and the fracture initiation/propagation toughness using the deformation fields in DIC analysis. Zhao et al. [41] analyzed the cracks' mechanism using the strain field around crack tips and summarized the crack evolution characteristics in the hydraulic fracturing process. Moreover, Miao et al. [42] distinguished the cracking process of flawed sandstone with different infilling materials by quantifying the displacement information between the observation points enclosing the flaws. To date, few indoor experiments have attempted to use the DIC technique to investigate the cracking behavior of flawed specimen in dynamic compression tests.

Therefore, the objective of this work is to provide a further understanding of the cracking behavior of single-flaw specimens under dynamic loading conditions. The open and closed flaws with different inclination angles were prefabricated in the cement mortar plate specimens, and the dynamic compression tests were carried out using a 50 mm diameter SHPB system. With the dynamic stress equilibrium achieved, the macroscopic strength characteristics of two types of specimens were investigated and presented in detail. During the dynamic loading, a high-resolution camera was arranged to capture the macroscopic cracking information, the crack patterns were subsequently identified and classified, and the cracking sequence and failure mode are also studied. In addition, the DIC technique was introduced to measure the surface deformation characteristics, based on which the stress field characteristics were quantitatively analyzed. In the last, the relationship among the nominal strength, crack type, and SIFs of the specimens with an open and closed flaw was discussed.

2. Experimental Program

2.1. Specimen Preparation. The rock-like plate specimens with desirable brittleness regarding the crack speed and loading rate were adopted in this study. The plates are made of cement, sand, and water with mass proportions of 1 : 3 : 0.57. The cement used was the ordinary Portland cement (62.5 Grade) with high-strength characteristics, and the sand

used was the ordinary sieved fine river sand with an average particle size less than 0.5 mm [25]. The mixture was first poured into a cement mixer and evenly stirred; then, a rod cement vibrator was used to promote the escape of air bubbles within the mixture, thereby making the mixture more homogenous. Afterward, the mixture was cast into the specialized plate mold, and an ultrathin metal (0.15 mm in thickness and 6 mm in length, dismantled from the specimens after the mixture is hardened) with different inclination angles was inserted into the mixture to simulate the open flaws. Correspondingly, the epoxy resin sheets of the same dimensions as that of the metal sheets were inserted to mimic the infilled flaws. The angles of the flaws varied from 0° to 90° at an interval of 15°. The cement mold was then placed in a curing box with a constant temperature of 20°C and relative humidity of 95%. The average final compressive strength and elastic modulus of the cement mixture after curing were 30 MPa and 23.63 GPa, respectively. Moreover, the elastic modulus of the epoxy resin is 0.12 GPa, which is much lower than that of the cement mixture. After curing, the cement mixture was carefully polished to the specimens with a dimension of 47 mm × 47 mm × 15 mm, as illustrated in Figure 1.

2.2. SHPB System and DIC Configurations. The dynamic compressive tests of the flawed specimens containing open and closed flaws were performed using a 50 mm diameter SHPB system (Figure 2).

The SHPB system mainly consists of a high-pressure gas gun system, a striker, an incident bar, a transmission bar, and a signal acquisition system. All the bars are made of high-strength maraging steel with a nominal yield strength of 2.5 GPa. Two sets of strain gauges attached at the center parts of the incident and transmitted bars in combination with the Wheatstone bridges are used to record the strain history during the dynamic loading. A high-speed Kirana camera was adopted to capture the images of the deformed specimen throughout the test, and two flashlights were placed nearby the camera to provide sufficient luminance on the specimen surface. The DIC technique is an optical method that uses the random natural or artificial speckle patterns on the specimen surface to obtain the full-field displacement information by matching the interrogated subsets before and after deformation, and the strain distribution can thus be derived using the specific algorithms [43, 44]. In this work, in order to achieve an optimal speckle pattern, the high-contrast speckles with an average size in the range of 4 to 5 pixels [45] were premade on the specimen surface as shown in Figure 2. The subset size in DIC analysis was chosen as 21 × 21 pixels. Prior to the dynamic loading, the resolution of the camera was set as 605 × 605 pixels for the frame rate of 1 000 000 fps and the corresponding interframe time was about 1.0 μs. The length to pixel ratio of the imaging system was calibrated as 0.0776 mm per pixel.

2.3. Data Measurement and Processing. Based on the strain history obtained by the strain gauges on the incident and transmitted bars, the stress on the two bar/specimen surfaces can be governed by

$$\begin{aligned} P_1(t) &= A_0 E_0 [\varepsilon_i(t) + \varepsilon_r(t)]; \\ P_2(t) &= A_0 E_0 \varepsilon_t(t), \end{aligned} \quad (1)$$

where E_0 is the elastic modulus of the bars; A_0 is the cross-sectional area of the bars. $P_1(t)$ and $P_2(t)$ refer to the stress on the incident and the transmitted bar ends. $\varepsilon_i(t)$, $\varepsilon_r(t)$, and $\varepsilon_t(t)$ denote the incident, reflected, and transmitted strain histories on the bars, respectively.

Typically, the stress equilibrium in the specimen before the dynamic failure is the fundamental prerequisite for the constitutive measurement of materials [46]. To meet this requirement, a pulse shaper made of C11000 copper disc was used to shape the waveform and a bell-shaped incident wave with a relatively long rising edge was generated, which provided sufficient time for the elastic wave to travel back and forth within the specimen for several times before the peak value, and thus the stress equilibrium (i.e., $P_1(t) \approx P_2(t) = P(t)$) could be easily achieved as shown in Figure 3.

With dynamic stress equilibrium achieved, the dynamic compressive stress/strain history of the specimen can be calculated by

$$\sigma(t) = \frac{P_1(t) + P_2(t)}{2A_s}, \quad (2)$$

$$\varepsilon(t) = \frac{C}{L_s} \int_0^t [\varepsilon_i(t) - \varepsilon_r(t) - \varepsilon_t(t)],$$

where A_s and L_s are the cross-section area and length of the specimen, respectively. C is the 1D elastic bar wave speed. Therefore, the effective dynamic compressive stress-strain curve can be obtained, and the nominal dynamic compressive strength, σ_c , can be attained by identifying the peak value of the stress-time curve. Moreover, the loading rate, characterized by $\dot{\sigma}$ and defined as the slope of the prepeak linear regime of the stress-time curve in Figure 3, was adopted in this work to study the rate-dependent behavior of compressive strength.

2.4. Determination of the Stress Field around the Crack Tip.

The accurate evaluation of the stress field around the crack tip is of great significance to reveal the cracking mechanism, among which the key problem is to determine the stress intensity factors (SIFs), K_I and K_{II} . To achieve this goal, an experimental approach using the DIC displacement field was adopted to calculate the SIFs. Specifically, assuming the origin of the polar coordinates coincides with the initial flaw tip and the x -axis is in the flaw plane, and ignoring the rigid body translation and rotation in the dynamic loading, the

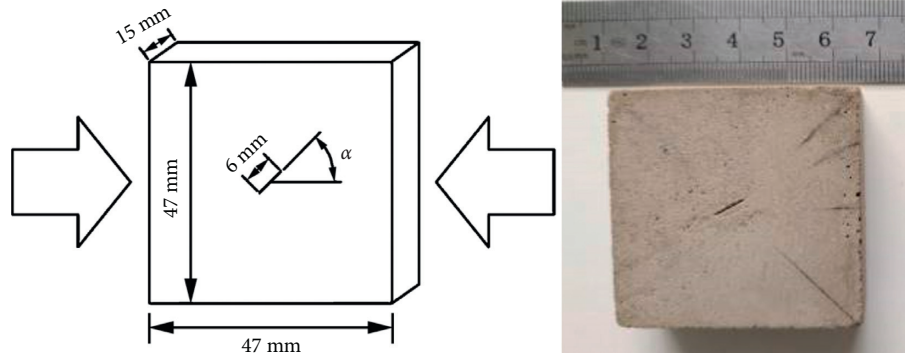


FIGURE 1: The geometry of the single-flaw specimen.

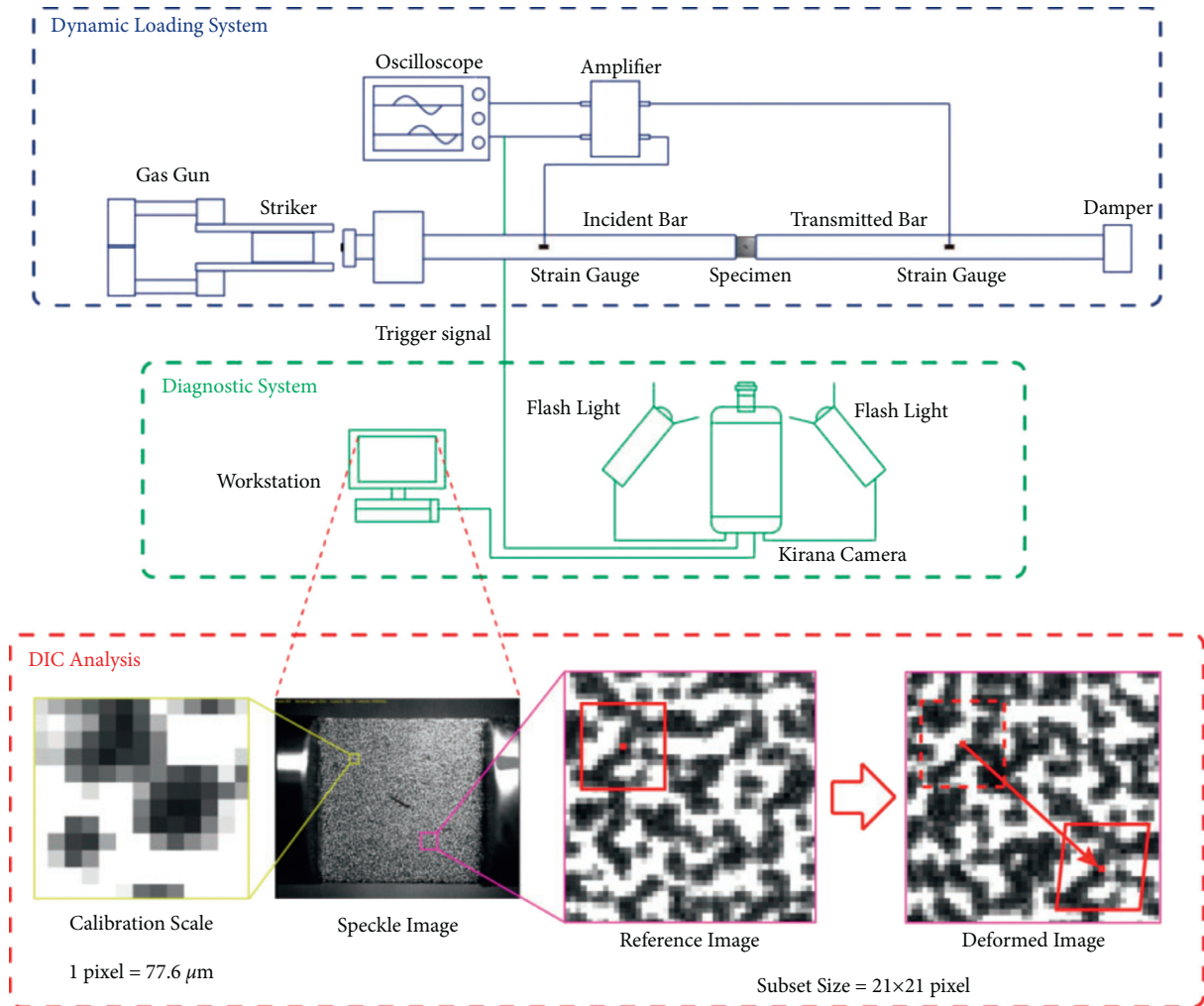


FIGURE 2: Schematics of the split Hopkinson pressure bar (SHPB) system with the DIC technique.

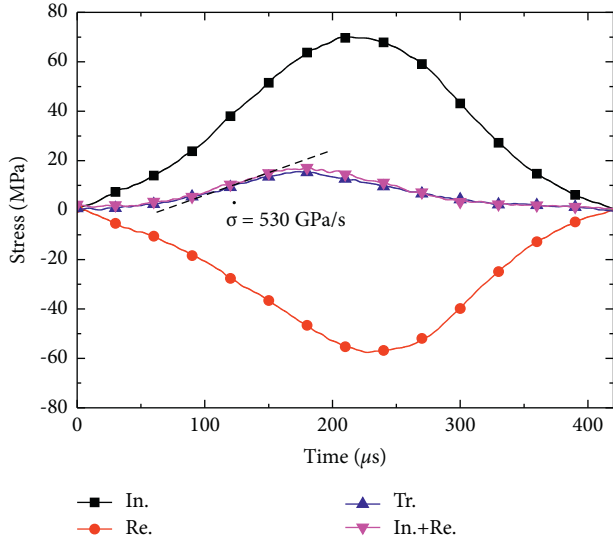


FIGURE 3: Dynamic stress equilibrium and the determination of the loading rate.

theoretical displacement fields around the tip of mode I, mode II, and mixed-mode fracture in plane problems can be written as [39, 47, 48]

$$u_k = \sum_{n=0}^N A_n f_{\text{I}}(r_k, \theta_k) - \sum_{n=0}^N B_n f_{\text{II}}(r_k, \theta_k), \quad (3)$$

$$v_k = \sum_{n=0}^N A_n g_{\text{I}}(r_k, \theta_k) - \sum_{n=0}^N B_n g_{\text{II}}(r_k, \theta_k), \quad (4)$$

where $f_{\text{I}}(r_k, \theta_k) = (r_k^{(n/2)}/2\mu)[(\kappa + (n/2) + (-1)^n)\cos(n/2)\theta_k - (n/2)\cos((n/2) - 2)\theta_k]$, $g_{\text{I}}(r_k, \theta_k) = (r_k^{(n/2)}/2\mu)[(\kappa + (n/2) - (-1)^n)\sin(n/2)\theta_k - (n/2)\sin((n/2) - 2)\theta_k]$, $f_{\text{II}}(r_k, \theta_k) = (r_k^{(n/2)}/2\mu)[(\kappa - (n/2) - (-1)^n)\sin(n/2)\theta_k + (n/2)\cos((n/2) - 2)\theta_k]$, $g_{\text{II}}(r_k, \theta_k) = (r_k^{(n/2)}/2\mu)[(\kappa - (n/2) + (-1)^n)\cos(n/2)\theta_k + (n/2)\cos((n/2) - 2)\theta_k]$.

u_k and v_k are the directional displacement component. μ and κ donate the shear modulus and Muskhelishvili's coefficient, respectively. r_k and θ_k are the polar coordinates around a tip. In particular, the coefficients of the first terms of parameters A_n and B_n are related to the mode I and mode II stress intensity factors [49]. k refers to the number of displacement data points around the crack tip.

If M points are selected in the flaw tip region and N terms are adopted in the calculation, equations (3)–(4) can be rewritten in the matrix form as

$$h = b\Delta, \quad (5)$$

$$\text{where } h = \begin{bmatrix} u_1 \\ \vdots \\ u_m \\ v_1 \\ \vdots \\ v_m \end{bmatrix}, b = \begin{bmatrix} f_{\text{II}} & \cdots & -f_{\text{III}} \\ \vdots & \ddots & \vdots \\ f_{\text{IM}} & \cdots & -f_{\text{IIM}} \\ g_{\text{II}} & \cdots & -g_{\text{III}} \\ \vdots & \ddots & \vdots \\ g_{\text{IM}} & \cdots & -g_{\text{IIM}} \end{bmatrix}, \Delta = \begin{bmatrix} A_1 \\ \vdots \\ A_m \\ B_1 \\ \vdots \\ B_m \end{bmatrix}.$$

Considering the full-field displacement information with subpixel accuracy of the points enclosing the flaw tip can be easily obtained in the DIC analysis and the location of the flaw tip before initiation is known, as long as the number of the selected displacement data points M exceeds the number of terms N , the coefficients A_n and B_n can be easily resolved through the nonlinear least-squares method using the MATLAB Software. Therefore, the mode I, mode II SIFs histories, and K_{I} and K_{II} at the crack initiation onset can be obtained as follows [47]

$$\begin{aligned} K_{\text{I}} &= \sqrt{2\pi}A_1, \\ K_{\text{II}} &= \sqrt{2\pi}B_1. \end{aligned} \quad (6)$$

It is noteworthy that, with the dynamic stress equilibrium achieved, the cracking behaviors of the two crack tips are similar and roughly symmetrical; hence, for simplicity purposes, only the stress intensity factors of the crack tip on the incident bar side are displayed in the following work.

3. Experimental Results

3.1. The Dynamic Mechanical Properties of Specimens with Open and Closed Flaws. Figure 4 shows the dynamic compressive stress-strain behavior of the specimen with 30° open and closed flaws.

Figure 5 depicts the nominal strength variations of the specimens with open and closed flaws, in which the black legends starting with the letter C refer to the specimens with a closed flaw. One can see that regardless of the flaw type, the nominal dynamic strength of the flawed specimens increases with the increase of the loading rate, and the strength of specimens with an open flaw is obviously lower than that of the specimens with a closed flaw at a similar loading rate, which is consistent with the results under static stress state [25]. Interestingly, the peak strain of specimens with an open flaw decreases with the increase of the loading rate, and the tangent modulus (the slope of the linear regime of the stress-strain curve) slightly increases whereas for specimens with a closed flaw, the peak strain increases with increasing the loading rate, and the tangent modulus is almost identical.

To investigate the influence of the flaw orientation on the nominal strength of the flawed specimen, the strength variations at similar loading rates, i.e., ~600, ~800, and ~1000 GPa/s, of specimens with both open and closed flaws are separately plotted in Figure 6.

As illustrated in Figure 6, the dynamic strength of both the two types of specimens exhibit an overall downward tendency with increasing the flaw angle except the strength values at the inclination of 30°; this result is mainly due to the high shear stress field of 30° sample, as shown in Section 3.3, it can be found that the shear stress of the 30° sample is the maximum, and the shear strength of the brittle material is greater than the tensile strength. Therefore, in the shear-dominated state, its strength will be improved. This phenomenon is similar to the results reported in the literature [50, 51] but slightly different from those in [5, 29], in which the static or dynamic strength monotonously decreases with

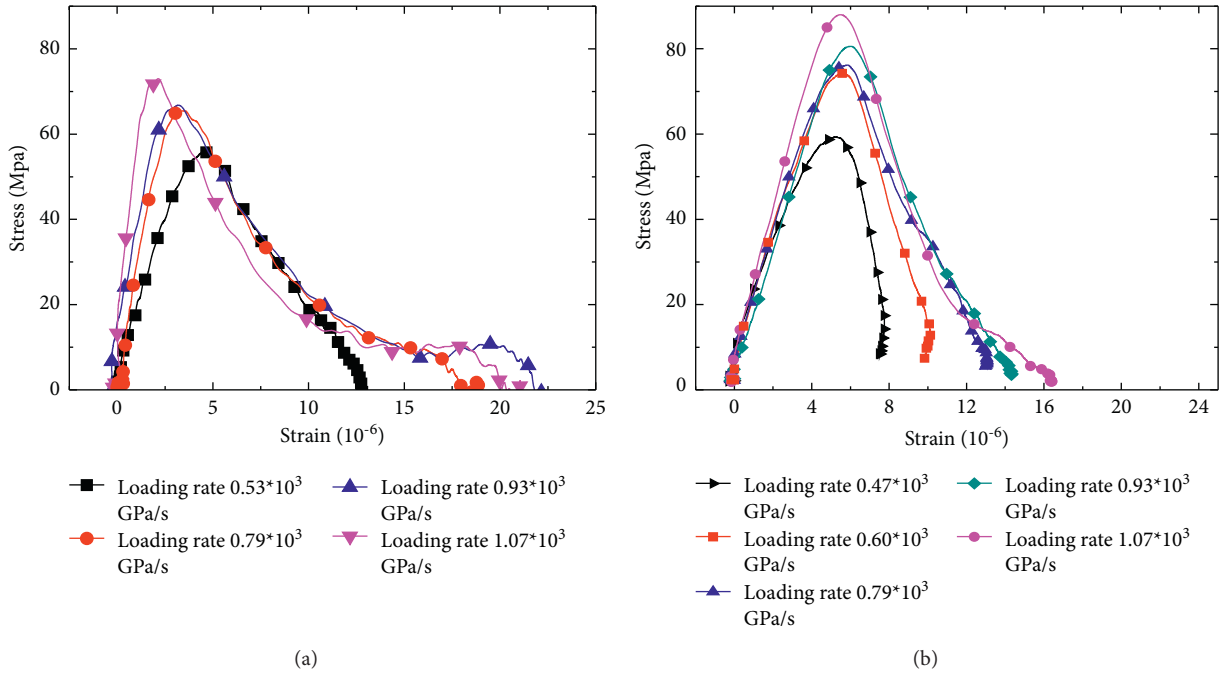


FIGURE 4: Dynamic stress-strain curves of specimens with 30° (a) open and (b) closed flaw.

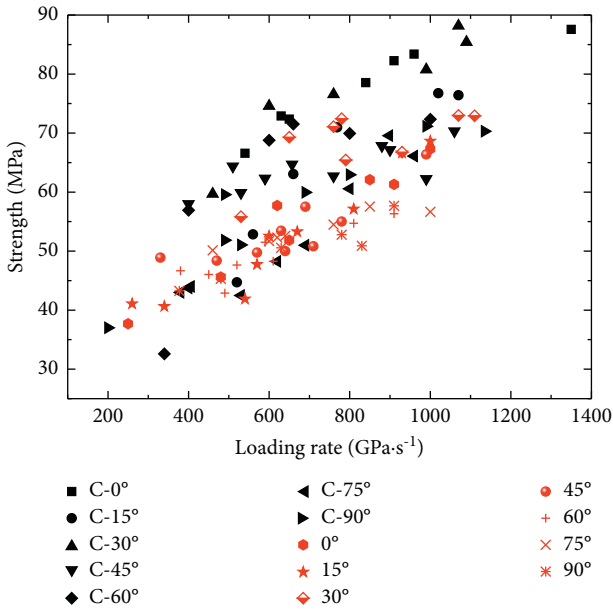


FIGURE 5: Dynamic compressive strength of specimens with various flaw angles (0~90°).

increasing the flaw inclination. This discrepancy can be attributed to the different rock types used in this work because whether the tensile cracks or shear cracks are primarily generated around the flaw tips relies on not only the specific stress field (dominated by the flaw geometry) but also the shear strength to tensile strength ratio (dominated mechanical properties of rocks) [52].

3.2. *Cracking Behavior and Failure Modes.* Figures 7 and 8 demonstrate the failure characteristics of the specimens with

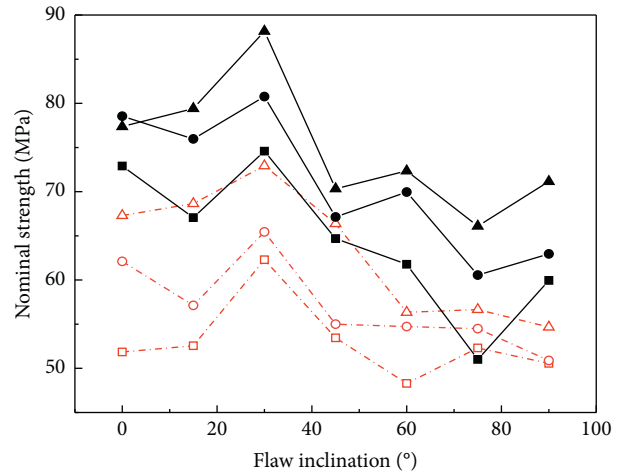


FIGURE 6: Variations of the nominal strength as a function of the flaw inclination angle.

different flaw properties at a similar loading rate (~600 GPa/s). Note that the relatively low resolution and weak contrast of image snapshots can hardly achieve the accurate characterization of the crack morphology; the vertical displacement distribution images are thus used as a complementary approach in this work. In the DIC images, the paths of the macroscopic cracks can be well distinguished by recognizing the dividing lines in the cloud maps. One can see that for specimens with an open flaw, four distinct cracks along the diagonal directions of the specimen are observed, and the macrofailure mode displays a typical

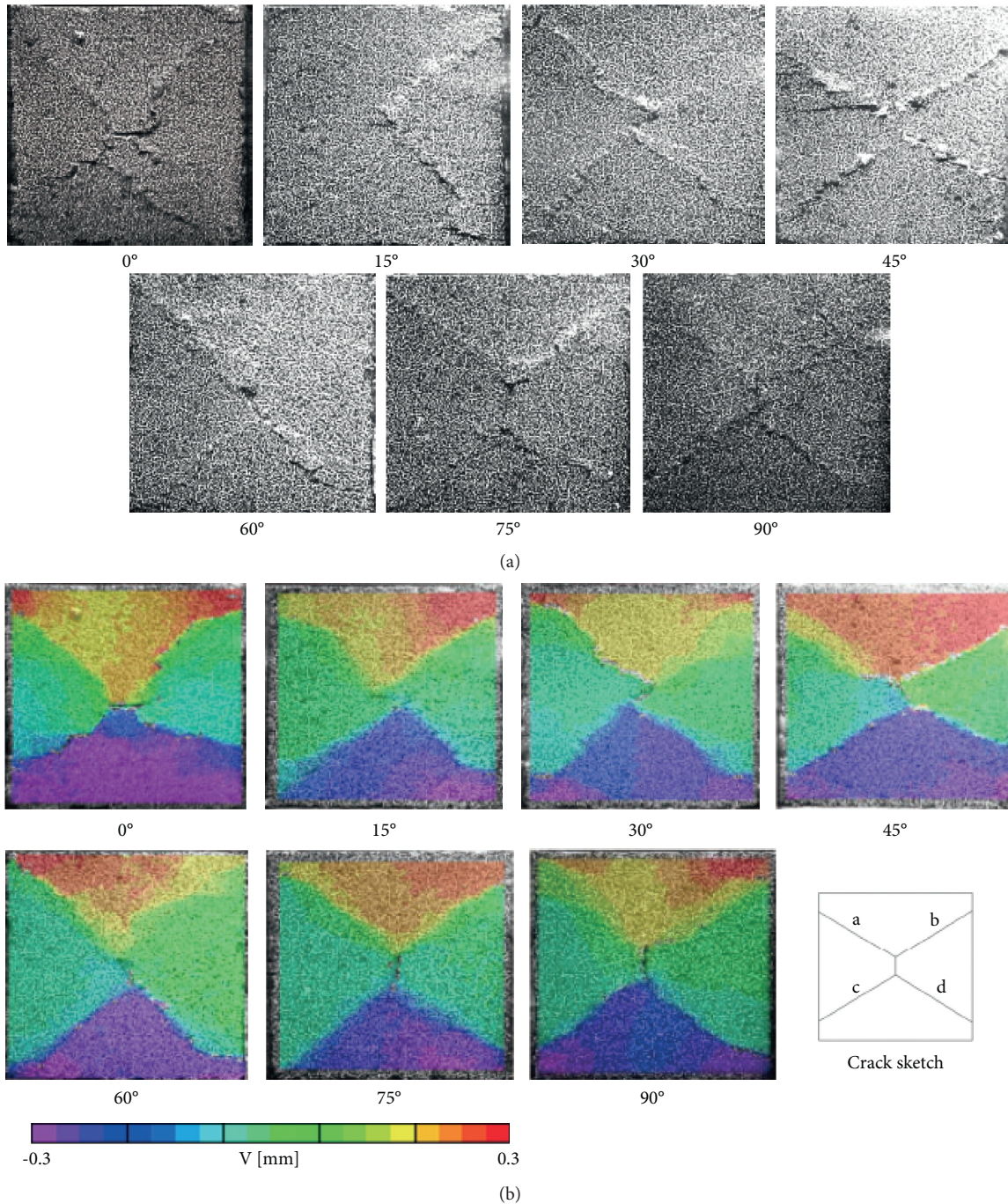


FIGURE 7: Failure characteristics of specimens containing an open flaw with different inclinations at a similar loading rate. (a) Image snapshots. (b) Vertical displacement distributions. Loading direction: from left to right.

X-shaped crack band regardless of the flaw inclination, which is consistent with the findings in [50, 51]. Under dynamic loading, the failure mode is fundamentally different from that under static loading, while the latter always shows a typical splitting failure mode with two identical halves due to the further development of the tensile wing cracks. In addition, the failure mode for specimens with a closed flaw is more complicated.

To achieve better visualization, the ultimate crack trajectories of the specimens with a closed flaw are sketched in Figure 9. In these sketches, the other observed macrocracks that are not directly involved in the ultimate failure are neglected and not shown. The main cracks are labeled by alphabets a~e, and it is observed that the macrocrack properties of the specimens vary with flaw inclination angles. Specifically, for 0° specimen, only two macrocracks

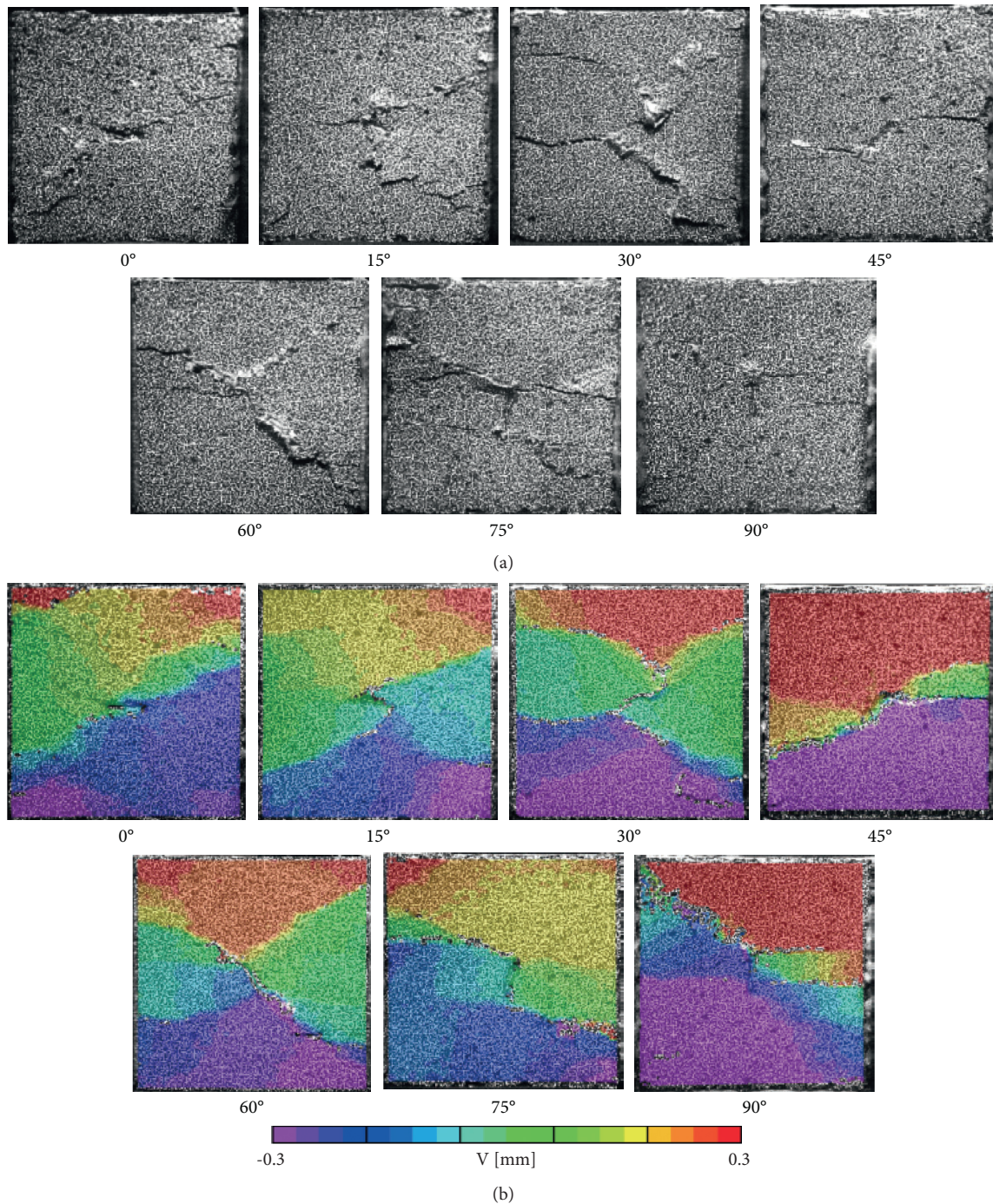


FIGURE 8: Typical failure characteristics of specimens containing a closed flaw with different inclinations at a similar loading rate. (a) Image snapshots. (b) Vertical displacement distributions. Loading direction: from left to right.

emanated from the flaw tips are observed, and as the inclination angle increased, both the crack types and crack density correspondingly increase, and the failure mode exhibits an atypical X-shaped form with four shear cracks emanating from the flaw tips but ending at the specimen edges near the horizontal centerline.

Based on the crack initiation/propagation mechanism and high-speed camera observations, and referring to the crack classification proposed by Wong and Einstein [53], only five crack types with different trajectories are identified and categorized for the specimens with two flaw types under dynamic loading. Note that these five crack types are

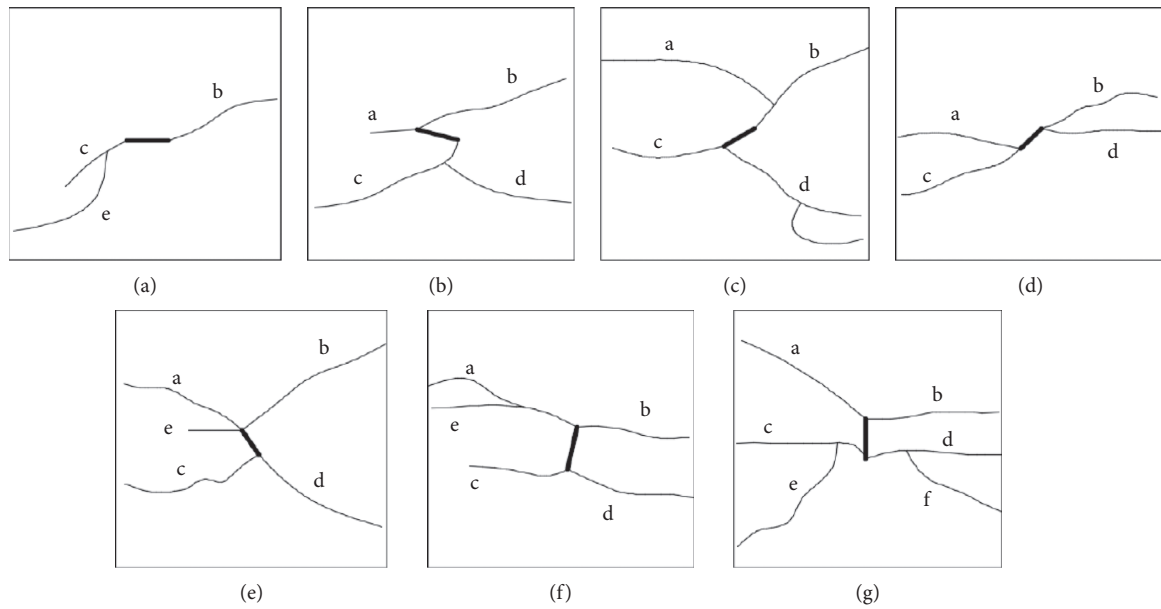


FIGURE 9: Schematic sketches of the failure patterns for specimens with a closed flaw at different inclinations. (a) 0° . (b) 15° . (c) 30° . (d) 45° . (e) 60° . (f) 75° . (g) 90° .

summarized by observing for the multiple specimens with the same flaw geometry, not only limited to the typical sketches in Figures 8 and 9. As schematically illustrated in Figure 10, two crack types are shear cracks (Type I and Type II), two are tensile cracks (Type III and Type IV), and the remaining one is a mixed shear-tensile crack (Type V).

The detailed descriptions of the crack types and occurrences are given as follows. *Type I*. Coplanar or quasi-coplanar shear cracks are commonly observed in specimens with low to intermediate inclination angles (from 0° to 60° , except for 0° specimen with an open flaw) regardless of infilling conditions, and the two cracks emanate simultaneously from the flaw tips. The main difference between the open and closed flaws is the extension angles, and the angles are much higher for open flaws than those for closed ones. Besides, the apparent surface crush and spalling phenomenon can be recognized in the snapshots recorded by the high-speed camera, which is an indication of high compression enclosing the crack plane [10]. *Type II*. Similar to the coplanar shear cracks, the oblique shear cracks also emanate simultaneously from the crack tips but propagate at a certain angle with respect to the flaw plane, accompanied by the surface crush and spalling. The coplanar shear cracks develop in almost all the specimens with a closed flaw but are absent for 75° and 90° specimens with an open flaw. *Type III*. The tensile wing crack is the most commonly observed first crack form in the uniaxial compressive test under static loads [53–56], which will further propagate as the loads continued and lead to the eventual splitting failure of the specimen. However, the wing tensile cracks only occur in the 0° and 15° specimens with an open flaw under dynamic loads in this study. *Type IV*. This type of cracks usually commences at or near the flaw types and propagates along the loading direction. The development of type IV crack is only generated in 75° and 90° specimens with an open flaw. *Type V*. The

mixed shear-tensile crack is recognized in the specimens with a closed flaw at higher inclination angles, which first generates near the flaw tips at a certain angle with respect to the flaw inclination accompanied by a small crushed zone, then gradually transforms to the tensile form, and extends toward the loading plate.

In order to well describe the cracking behavior of specimens under dynamic loading conditions, the information of the crack types and the cracking sequence before failure onset of typical specimens are summarized in Table 1. It is noteworthy that only four main cracks in different quadrants that initiate at the crack tips (a~d, as depicted in Figures 7 and 9) are considered for comparison purposes. One can see that the shear cracks are the prevailing crack forms in dynamic tests for both the open and resin-infilled flaws, whereas the tensile cracks only generate around the open flaws with relatively high (75° and 90°) or low (0° and 15°) inclinations, indicating that the development of tensile crack is suppressed in dynamic loading, particularly for the specimens with a closed flaw. This agrees well with the previous findings [50, 51, 54]. Besides, for specimens with shear-dominated failure mode (e.g., 30° to 60° for the open flaw and all for the closed flaw), type I shear cracks are always observed as the first crack, whereas for specimens with tensile dominated (90° open flaw) or mixed tensile-shear (0° , 15° and 75° open flaw) failure modes, the involved tensile cracks generate earlier than the shear cracks. Additionally, in accordance with the identified crack types at the failure onset, it is found that specimens with an open flaw first transform from the tensile-shear mixed mode to shear-dominant and eventually to the tensile-dominant failure mode. Considering the tensile strength is always smaller than its shear strength, the failure mode transition well explains the macroscopic dynamic strength characteristics, that is, increasing first and then decreasing with the flaw inclination angle.

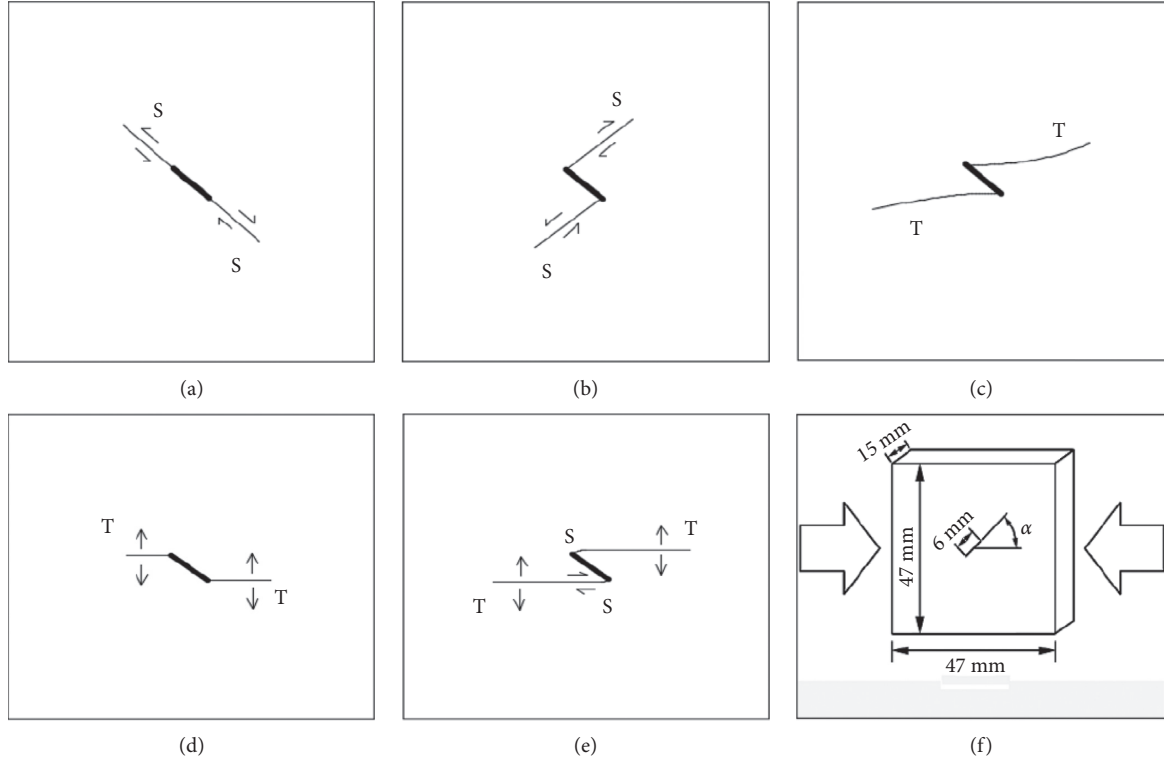


FIGURE 10: Five crack types initiated from the preexisting flaws identified in dynamic tests. (a) Type I: coplanar shear crack. (b) Type II: oblique shear crack. (c) Type III: tensile wing crack. (d) Type IV: tensile crack. (e) Type V: mixed shear-tensile crack. (f) Schematic diagram of experimental sample size.

TABLE 1: Crack type and cracking sequence.

Specimen type	Crack types					Cracking sequence
	Type I shear	Type II shear	Type III tensile	Type IV tensile	Type V mixed mode	
0°		a, d	b, c ¹			c - d - b - a
15°	b, c		a, d ¹			d - b, c - a
30°	b ¹ , c ¹	a, d				b, c - a, d
45°	a ¹ , d	b, c				a - b - d - c
60°	a ¹ , d ¹	b, c				a, d - b - c
75°	b ¹ , c			a ¹ , d		a, b - d - c
90°				a, b ¹ , c ¹ , d		b, c - a, d
0° (C)	b ¹ , c					b - c
15° (C)	a ¹ , d ¹	b, c				a, d - b - c
30° (C)	b ¹ , c	a, d				b - d - c - a
45° (C)	b ¹ , c ¹	a, d				b, c - d - a
60° (C)	a ¹ , d ¹	b, c				a, d - b, c
75° (C)		b, c			a, d ¹	d - a - b, c
90° (C)		b ¹ , c			a, d ¹	b, d - a - c

Note. a¹ indicates that the crack labeled by alphabet a is the first crack observed before failure.

3.3. Stress Field Characteristics around the Flaw Tip. Figures 11 and 12 show the tensile and shear stress intensity factors (K_I and K_{II}) at the crack initiation onset as a function of the loading rate. The crack initiation onset can be determined by directly reading the time corresponding to the first peak point of the SIF history curves [39]. It is found that both K_I and K_{II} obviously increase with the increase of the loading rate, regardless of the flaw angle and the infilling conditions. Note that the results of 90° specimens are excluded because the first cracks always initiate at the center of

the flaws rather than the tips, which is consistent with those observations in literature [54, 57]. Although there is wide scatter in the data, the values of the tensile and shear stress intensity factors still demonstrate a remarkable inclination-dependent behavior.

The K_I and K_{II} of specimens with open and closed flaws at the loading rates of ~ 600 GPa/s and ~ 800 GPa/s are plotted in Figure 13 for better illustration. Specifically, for the specimens with an open flaw, K_I decreases first and reaches the lowest value at 30° and then obviously increases

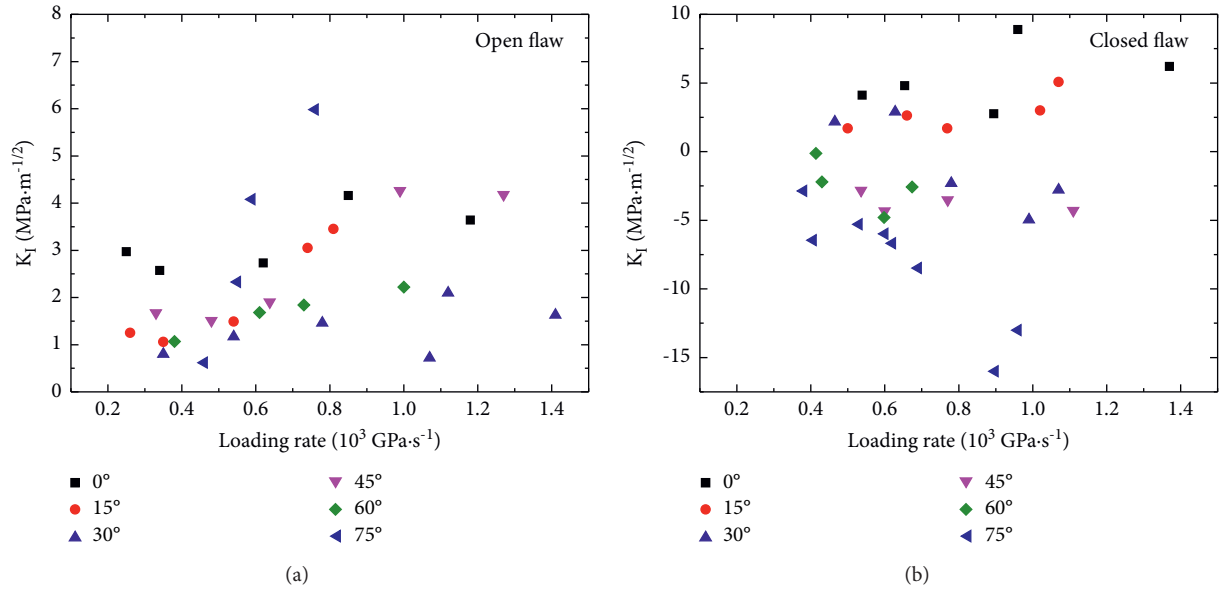


FIGURE 11: Variations of K_I at the tips of (a) open and (b) closed flaws with different angles versus the loading rate.

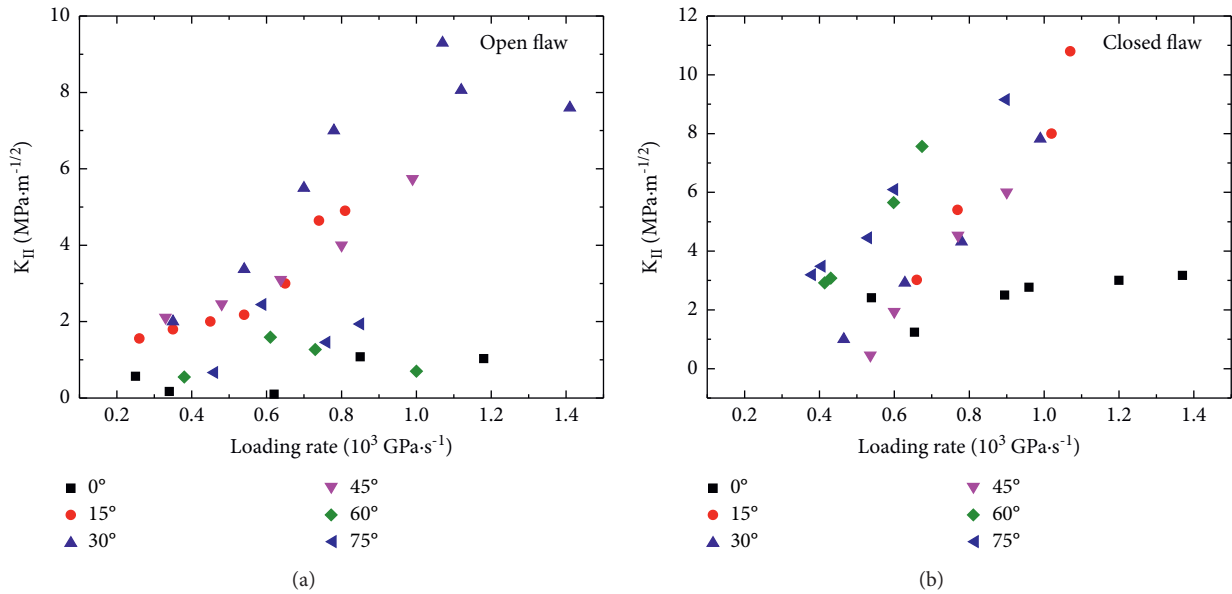


FIGURE 12: Variations of K_{II} at the tips of (a) open and (b) closed flaws with different angles versus the loading rate.

with the increase of the inclination angle whereas K_{II} exhibits an entirely contrary tendency, increasing first to 30° with a maximum magnitude of $6.9 \text{ MPa}/\text{m}^{0.5}$ and then decreasing to nearly $1.0 \text{ MPa}/\text{m}^{0.5}$ at 75° (Figure 13(a)). This phenomenon indicates that, as the inclination angles increase, the stress field at the flaw tip at the initiation onset experiences the tensile stress dominant to the shear stress dominant and then returns back the tensile stress dominant process. For the specimens with a closed flaw, the tensile stress intensity factor K_I decreases with increasing the inclination angle. One can find that the K_I values at higher loading rates are negative, indicating that the compressive stress occurs around the crack tips and the tensile cracks are

thus suppressed. Correspondingly, K_{II} values significantly increase with the inclination angle (Figure 13(b)), suggesting that the shear stress field becomes dominant around the closed flaw tips and the shear crack may be preferentially produced as the first crack.

4. Discussion

It can be observed that the macroscopic strength, crack types, and SIFs are found to be strongly dependent on the infilling conditions, loading rate, and flaw inclination angle. For a given loading rate, the nominal strength of a closed flaw is higher than that of an open flaw, mainly attributed to

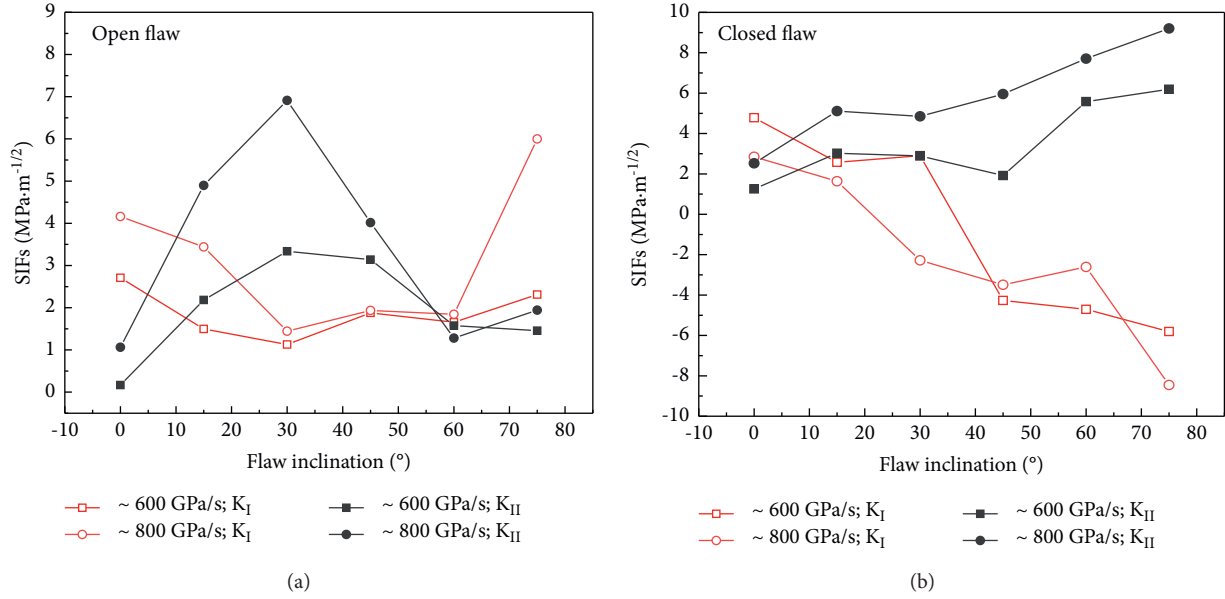


FIGURE 13: Variations of K_I and K_{II} as a function of the flaw inclination angle.

the friction effect induced by the infilling material. Specifically, the shear force around the crack tips should be large enough to overcome the friction before mobilizing the sliding of flaw faces; thus, an extra external load is demanded and higher strength is introduced for the closed flaw. Besides, the crack type that first appears during the dynamic loading is also closely related to the friction effect between the flaw surfaces, since the friction coefficient can significantly affect the stress field around the flaw tip [52]. In general, the larger the friction coefficient of the infilling material is, the more likely the shear failure occurs. This phenomenon is also experimentally demonstrated by Miao et al. [42]. Therefore, the infilling conditions play a significant role in determining the strength and cracking behaviors.

Moreover, one can find that the variations of SIFs show rather different tendencies for specimens with an open flaw and closed flaw. For specimens with an open flaw, either tensile cracks or shear cracks occur first depending on the flaw inclination angle. Specifically, when the flaw inclination is lower or higher (0° , 60° , and 75°), the mode I stress intensity factor K_I is slightly greater than mode II stress intensity factor K_{II} , indicating the tensile cracks are more likely generated because the tensile strength of rock is generally smaller than its shear strength. This is basically compatible with the crack types identified in Figure 7 and Table 1. The tensile or tensile-shear mixed failure mode leads to a lower nominal strength compared with that induced by the shear failure mode. When the inclination angle lies between 15° and 45° , the stress intensity factor K_{II} is apparently larger than K_I , and the shear crack may be preferentially produced as the primary pattern, resulting in higher nominal strength. It is worth noting that a higher K_{II} does not indicate that the first crack must occur in the form of the shear crack, since in such cases the crack type primarily depends on the ratio of shear to tensile strength.

For specimens with a closed flaw, K_I exhibits a linear downward tendency and changes from positive to negative at the angle of 30° . The negative value of K_I means that the crack tip is under compression and only shear crack initiation is possible under this condition, which is proved by the observations of the crack types in Figure 8. Besides, the K_{II} increases monotonously as the flaw inclination angle increased, and this is because the frictional force continues to increase under the action of the gradually increased normal stress component perpendicular to the flaw plane. However, the nominal strength shows a reverse trend, implying that these two quantities are not directly correlated. In other words, a higher mode II stress intensity in the close vicinity of the crack tip at crack initiation onset does not mean a correspondingly higher macroscopic strength; the characteristics of secondary cracks and the coalescence behavior of the first and secondary cracks also significantly contribute to the macroscopic mechanical properties of flawed rocks.

5. Conclusions

In this study, an attempt is made to investigate the mechanical and cracking behavior of specimens with single open and closed flaws under dynamic loading conditions. The effects of the flaw inclination angle, loading rate, and infilling conditions are carefully considered, and the stress intensity factors are obtained in accordance with the DIC results. The conclusions are summarized as follows:

- (1) The dynamic nominal strength of both two types of specimens shows similar loading rate and flaw angle dependency, almost linearly increasing with the increase of the loading rate, whereas increasing first and then decreasing with the inclination angle. At a similar loading rate, the dynamic strength of specimens with a closed flaw is higher than that with an

open flaw. The infilling conditions play a significant role in determining the macroscopic strength.

- (2) The type and inclination angle of preexisting flaws significantly influence both the dynamic crack behavior and the failure mode. Specifically, the shear cracks are preferentially generated as the primary pattern for the open flaw with intermediate inclination angles, whereas shear cracks are the most common form for the closed flaw regardless of the inclination angle. The failure pattern of specimens with an open flaw is mainly X-shaped tensile or tensile-shear mixed mode, whereas the closed flawed specimens always fail in the form of an atypical X-shaped shear mode.
- (3) The stress intensity factors K_I and K_{II} of the open and closed flaws exhibit obviously different behaviors, and the variations of these two stress intensity factors can be used to predict the first crack types. The predictions are roughly compatible with those observed from the snapshots recorded by the high-speed camera. Besides, the stress intensity factors are also flaw inclination- and rate-dependent. Furthermore, the differences in the macroscopic strength, cracking behavior, and stress intensity factors between the closed and open flaws are mainly attributed to the friction effect on the flaw surface.

Data Availability

All data generated or used during the study are available from the corresponding author by request.

Conflicts of Interest

The authors declare that they have no conflicts of interest.

Acknowledgments

This work was supported by the Hebei Natural Science Foundation (E2020208071), the Hebei Provincial Department of Education for cultivating the innovative ability of postgraduate student project (CXZZSS2022085), the 03 Special and 5G Projects in Jiangxi Province (20203-ABC03B05), and the Open Research Topics of State Key Laboratory of Mechanical Behavior and System Safety of Traffic Engineering Structures (KF2020-08).

References

- [1] A. Palmström, V. Sharma, and K. Saxena, *In-situ Characterization of Rocks*, Balkema Publication, Avereest, Netherlands, 2001.
- [2] M. Sagong and A. Bobet, "Coalescence of multiple flaws in a rock-model material in uniaxial compression," *International Journal of Rock Mechanics and Mining Sciences*, vol. 39, no. 2, pp. 229–241, 2002.
- [3] B. Shen, O. Stephansson, H. H. Einstein, and B. Ghahreman, "Coalescence of fractures under shear stresses in experiments," *Journal of Geophysical Research: Solid Earth*, vol. 100, no. B4, pp. 5975–5990, 1995.
- [4] R. H. C. Wong and K. T. Chau, "Crack coalescence in a rock-like material containing two cracks," *International Journal of Rock Mechanics and Mining Sciences*, vol. 35, no. 2, pp. 147–164, 1998.
- [5] Y. Wang, H. Zhang, H. Lin, Y. Zhao, and Y. Liu, "Fracture behaviour of central-flawed rock plate under uniaxial compression," *Theoretical and Applied Fracture Mechanics*, vol. 106, Article ID 102503, 2020.
- [6] K. Zhang, Y. Chen, W. Fan, X. Liu, H. Luan, and J. Xie, "Influence of intermittent artificial crack density on shear fracturing and fractal behavior of rock bridges: experimental and numerical studies," *Rock Mechanics and Rock Engineering*, vol. 53, no. 2, pp. 553–568, 2020.
- [7] T. Y. Ko, H. Einstein, and J. Kemeny, "Crack coalescence in brittle material under cyclic loading," in *Proceedings of the Golden Rocks 2006, The 41st US Symposium on Rock Mechanics (USRMS)*, American Rock Mechanics Association, Golden, CO, USA, June 2006.
- [8] B. Shen, "The mechanism of fracture coalescence in compression-experimental study and numerical simulation," *Engineering Fracture Mechanics*, vol. 51, no. 1, pp. 73–85, 1995.
- [9] C. H. Park and A. Bobet, "Crack coalescence in specimens with open and closed flaws: a comparison," *International Journal of Rock Mechanics and Mining Sciences*, vol. 46, no. 5, pp. 819–829, 2009.
- [10] C. H. Park and A. Bobet, "Crack initiation, propagation and coalescence from frictional flaws in uniaxial compression," *Engineering Fracture Mechanics*, vol. 77, no. 14, pp. 2727–2748, 2010.
- [11] X.-P. Zhang and L. N. Y. Wong, "Cracking processes in rock-like material containing a single flaw under uniaxial compression: a numerical study based on parallel bonded-particle model approach," *Rock Mechanics and Rock Engineering*, vol. 45, pp. 711–737, 2012.
- [12] A. Bobet and H. H. Einstein, "Fracture coalescence in rock-type materials under uniaxial and biaxial compression," *International Journal of Rock Mechanics and Mining Sciences*, vol. 35, no. 7, pp. 863–888, 1998.
- [13] H. Jiefan, C. Ganglin, Z. Yonghong, and W. Ren, "An experimental study of the strain field development prior to failure of a marble plate under compression," *Tectonophysics*, vol. 175, no. 1-3, pp. 269–284, 1990.
- [14] R. H. C. Wong, K. T. Chau, C. A. Tang, and P. Lin, "Analysis of crack coalescence in rock-like materials containing three flaws-Part I: experimental approach," *International Journal of Rock Mechanics and Mining Sciences*, vol. 38, no. 7, pp. 909–924, 2001.
- [15] Y.-H. Huang, S.-Q. Yang, and W.-L. Tian, "Crack coalescence behavior of sandstone specimen containing two pre-existing flaws under different confining pressures," *Theoretical and Applied Fracture Mechanics*, vol. 99, pp. 118–130, 2019.
- [16] X. Liu, Q. Liu, B. Liu, Y. Zhu, and P. Zhang, "Failure behavior for rocklike material with cross crack under biaxial compression," *Journal of Materials in Civil Engineering*, vol. 31, no. 2, 2019.
- [17] N. H. T. Nguyen, H. H. Bui, G. D. Nguyen, and J. Kodikara, "A cohesive damage-plasticity model for DEM and its application for numerical investigation of soft rock fracture properties," *International Journal of Plasticity*, vol. 98, pp. 175–196, 2017.
- [18] H. Lee and S. Jeon, "An experimental and numerical study of fracture coalescence in pre-cracked specimens under uniaxial compression," *International Journal of Solids and Structures*, vol. 48, no. 6, pp. 979–999, 2011.

- [19] W. Wang, S. Sun, H. Le et al., "Experimental and numerical study on failure modes and shear strength parameters of rock-like specimens containing two infilled flaws," *International Journal of Civil Engineering*, vol. 17, no. 12, pp. 1895–1908, 2019.
- [20] X.-P. Zhang and L. N. Y. Wong, "Crack initiation, propagation and coalescence in rock-like material containing two flaws: a numerical study based on bonded-particle model approach," *Rock Mechanics and Rock Engineering*, vol. 46, no. 5, pp. 1001–1021, 2013.
- [21] H. Li and L. N. Y. Wong, "Influence of flaw inclination angle and loading condition on crack initiation and propagation," *International Journal of Solids and Structures*, vol. 49, no. 18, pp. 2482–2499, 2012.
- [22] S.-Q. Yang, Y.-H. Huang, and P. G. Ranjith, "Failure mechanical and acoustic behavior of brine saturated-sandstone containing two pre-existing flaws under different confining pressures," *Engineering Fracture Mechanics*, vol. 193, pp. 108–121, 2018.
- [23] H. Le, S. Sun, P. H. S. W. Kulatilake, and J. Wei, "Effect of grout on mechanical properties and cracking behavior of rock-like specimens containing a single flaw under uniaxial compression," *International Journal of Geomechanics*, vol. 18, no. 10, Article ID 04018129, 2018.
- [24] H. Le, S. Sun, and J. Wei, "Influence of types of grouting materials on compressive strength and crack behavior of rocklike specimens with single grout-infilled flaw under axial loads," *Journal of Materials in Civil Engineering*, vol. 31, no. 1, Article ID 06018022, 2019.
- [25] X. Zhuang, J. Chun, and H. Zhu, "A comparative study on unfilled and filled crack propagation for rock-like brittle material," *Theoretical and Applied Fracture Mechanics*, vol. 72, pp. 110–120, 2014.
- [26] A. Lavrov, "Kaiser effect observation in brittle rock cyclically loaded with different loading rates," *Mechanics of Materials*, vol. 33, no. 11, pp. 669–677, 2001.
- [27] X.-P. Zhang and L. N. Y. Wong, "Loading rate effects on cracking behavior of flaw-contained specimens under uniaxial compression," *International Journal of Fracture*, vol. 180, no. 1, pp. 93–110, 2013.
- [28] J.-Z. Zhang, X.-P. Zhou, J.-Y. Zhu, C. Xian, and Y.-T. Wang, "Quasi-static fracturing in double-flawed specimens under uniaxial loading: the role of strain rate," *International Journal of Fracture*, vol. 211, no. 1-2, pp. 75–102, 2018.
- [29] D. Li, Z. Han, X. Sun, T. Zhou, and X. Li, "Dynamic mechanical properties and fracturing behavior of marble specimens containing single and double flaws in SHPB tests," *Rock Mechanics and Rock Engineering*, vol. 52, no. 6, pp. 1623–1643, 2019.
- [30] H. Wang, A. Dyskin, E. Pasternak, and P. Dight, "3D crack growth in biaxial compression: influence of shape and inclination of initial cracks," *Rock Mechanics and Rock Engineering*, vol. 53, pp. 1–23, 2020.
- [31] X. P. Zhou, H. Cheng, and Y. F. Feng, "An experimental study of crack coalescence behaviour in rock-like materials containing multiple flaws under uniaxial compression," *Rock Mechanics and Rock Engineering*, vol. 47, no. 6, pp. 1961–1986, 2014.
- [32] T. L. Nguyen, S. A. Hall, P. Vacher, and G. Viggiani, "Fracture mechanisms in soft rock: identification and quantification of evolving displacement discontinuities by extended digital image correlation," *Tectonophysics*, vol. 503, no. 1-2, pp. 117–128, 2011.
- [33] C. A. Tang and S. Q. Kou, "Crack propagation and coalescence in brittle materials under compression," *Engineering Fracture Mechanics*, vol. 61, no. 3-4, pp. 311–324, 1998.
- [34] C. A. Tang, P. Lin, R. H. C. Wong, and K. T. Chau, "Analysis of crack coalescence in rock-like materials containing three flaws-Part II: numerical approach," *International Journal of Rock Mechanics and Mining Sciences*, vol. 38, no. 7, pp. 925–939, 2001.
- [35] X.-p. Zhang, Q. Zhang, and S. Wu, "Acoustic emission characteristics of the rock-like material containing a single flaw under different compressive loading rates," *Computers and Geotechnics*, vol. 83, pp. 83–97, 2017.
- [36] Z. Moradian, H. H. Einstein, and G. Ballivy, "Detection of cracking levels in brittle rocks by parametric analysis of the acoustic emission signals," *Rock Mechanics and Rock Engineering*, vol. 49, no. 3, pp. 785–800, 2016.
- [37] R. H. C. Wong, Y. S. H. Guo, K. T. Chau, W. S. Zhu, and S. C. Li, "The crack growth mechanism from 3-D surface flaw with strain and acoustic emission measurement under axial compression," *Key Engineering Materials*, vol. 353-358, pp. 2357–2360, 2007.
- [38] X.-P. Zhou, J.-Z. Zhang, and F. Berto, "Fracture analysis in brittle sandstone by digital imaging and AE techniques: role of flaw length ratio," *Journal of Materials in Civil Engineering*, vol. 32, no. 5, Article ID 04020085, 2020.
- [39] G. Gao, S. Huang, K. Xia, and Z. Li, "Application of digital image correlation (DIC) in dynamic notched semi-circular bend (NSCB) tests," *Experimental Mechanics*, vol. 55, no. 1, pp. 95–104, 2015.
- [40] G. Gao, W. Yao, K. Xia, and Z. Li, "Investigation of the rate dependence of fracture propagation in rocks using digital image correlation (DIC) method," *Engineering Fracture Mechanics*, vol. 138, pp. 146–155, 2015.
- [41] C. Zhao, J. Xing, Y. Zhou, Z. Shi, and G. Wang, "Experimental investigation on hydraulic fracturing of granite specimens with double flaws based on DIC," *Engineering Geology*, vol. 267, Article ID 105510, 2020.
- [42] S. Miao, P.-Z. Pan, Z. Wu, S. Li, and S. Zhao, "Fracture analysis of sandstone with a single filled flaw under uniaxial compression," *Engineering Fracture Mechanics*, vol. 204, pp. 319–343, 2018.
- [43] B. Pan, A. Asundi, H. Xie, and J. Gao, "Digital image correlation using iterative least squares and pointwise least squares for displacement field and strain field measurements," *Optics and Lasers in Engineering*, vol. 47, no. 7-8, pp. 865–874, 2009.
- [44] B. Pan, H. Xie, Z. Guo, and T. Hua, "Full-field strain measurement using a two-dimensional Savitzky-Golay digital differentiator in digital image correlation," *Optical Engineering*, vol. 46, no. 3, Article ID 033601, 2007.
- [45] M. A. Sutton, J. J. Orteu, and H. Schreier, *Image Correlation for Shape, Motion and Deformation Measurements: Basic Concepts, Theory and Applications*, Springer Science & Business Media, Heidelberg, Germany, 2009.
- [46] Y. X. Zhou, K. Xia, X. B. Li et al., "Suggested methods for determining the dynamic strength parameters and mode-I fracture toughness of rock materials," *International Journal of Rock Mechanics and Mining Sciences*, vol. 49, pp. 105–112, 2012.
- [47] S. Yoneyama, Y. Morimoto, and M. Takashi, "Automatic evaluation of mixed-mode stress intensity factors utilizing digital image correlation," *Strain*, vol. 42, no. 1, pp. 21–29, 2006.

- [48] R. Zhang and L. He, "Measurement of mixed-mode stress intensity factors using digital image correlation method," *Optics and Lasers in Engineering*, vol. 50, no. 7, pp. 1001–1007, 2012.
- [49] F. Liu, H. Zheng, and X. Du, "Hybrid analytical and MLS-based NMM for the determination of generalized stress intensity factors," *Mathematical Problems in Engineering*, vol. 2015, Article ID 219657, 9 pages, 2015.
- [50] X. Li, T. Zhou, and D. Li, "Dynamic strength and fracturing behavior of single-flawed prismatic marble specimens under impact loading with a split-hopkinson pressure bar," *Rock Mechanics and Rock Engineering*, vol. 50, no. 1, pp. 29–44, 2017.
- [51] C. Zou and L. N. Y. Wong, "Experimental studies on cracking processes and failure in marble under dynamic loading," *Engineering Geology*, vol. 173, pp. 19–31, 2014.
- [52] S. B. Tang, "The effect of T-stress on the fracture of brittle rock under compression," *International Journal of Rock Mechanics and Mining Sciences*, vol. 79, pp. 86–98, 2015.
- [53] L. N. Y. Wong and H. H. Einstein, "Systematic evaluation of cracking behavior in specimens containing single flaws under uniaxial compression," *International Journal of Rock Mechanics and Mining Sciences*, vol. 46, no. 2, pp. 239–249, 2009.
- [54] C. Zou, L. N. Y. Wong, J. J. Loo, and B. S. Gan, "Different mechanical and cracking behaviors of single-flawed brittle gypsum specimens under dynamic and quasi-static loadings," *Engineering Geology*, vol. 201, pp. 71–84, 2016.
- [55] E. Z. Lajtai, "A theoretical and experimental evaluation of the Griffith theory of brittle fracture," *Tectonophysics*, vol. 11, no. 2, pp. 129–156, 1971.
- [56] A. R. Ingraffea and F. E. Heuze, "Finite element models for rock fracture mechanics," *International Journal for Numerical and Analytical Methods in Geomechanics*, vol. 4, no. 1, pp. 25–43, 1980.
- [57] L. N. Wong and H. Einstein, "Fracturing behavior of prismatic specimens containing single flaws," in *Proceedings of the Golden rocks 2006, the 41st US symposium on rock mechanics (USRMS)*, American Rock Mechanics Association, Golden, Colorado, June 2006.